

Effects of DLP 3D Printing Conditions on Strength and Fracture Toughness of Al₂O₃/ZrO₂ Ceramics

Zdeněk Chlup^{1*}, Přemysl Šťastný², Hynek Hadraba¹, Filip Šiška¹, Luca Bertolla¹, Oldřich Ševeček³, Vojtěch Mařák², Daniel Drdlík^{2,3}

¹ Institute of Physics of Materials of the Czech Academy of Sciences, Žitkova 513/22, 616 00 Brno, Czech Republic

² CEITEC BUT, Brno University of Technology, Purkyňova 123, 612 00 Brno, Czech Republic

³ Faculty of Mechanical Engineering, Brno University of Technology, Technická 2, 616 69 Brno, Czech Republic

Abstract

Vat photopolymerisation via digital light processing enables fabrication of complex ceramic components, but mechanical reliability is limited by defects and anisotropy. This study evaluates the effects of curing energy, printing orientation, and multimaterial processing on flexural strength and fracture toughness of alumina and Al₂O₃/ZrO₂ laminates. An optimal curing energy of 200 mJ/cm² maximised green strength (15 MPa) while minimising lateral overpolymerisation. Sintered alumina showed orientation-dependent behaviour, with Weibull strengths of 359 MPa (horizontal) and 345 MPa (vertical) and Weibull moduli of 7.6 and 23.3, indicating differing flaw populations and scatter. Fracture toughness peaked for cracks propagating perpendicular to layers ($K_{Ic} \approx 4.9 \text{ MPa}\cdot\text{m}^{0.5}$). Fractography revealed failure dominated by surface and interlayer defects, including pores and cracks, with a bimodal flaw distribution. Multimaterial Al₂O₃/ZrO₂ laminates exceeded 700 MPa strength due to zirconia reinforcement and residual stresses, though cross-contamination and layer defects remain key limitations to reliability.

Keywords: DLP 3D printing; Fractography; Flexural strength; Fracture toughness; Ceramics

Introduction

Over the past few decades, ceramic materials have undergone significant development in materials science, fracture mechanics, fractographic analysis, and manufacturing technologies, resulting in substantial improvements in performance and reliability. In contrast, additive manufacturing (AM) offers unique design freedom by enabling the fabrication of highly complex near-net shapes beyond the reach of conventional methods, yet it remains limited in achieving the same level of material quality and consistency as classical approaches [1].

Nevertheless, AM of ceramics is becoming a significant technology for rapid prototyping, the production of small-batch structural components, and the customisation of medical implants [2-4]. The most commonly used approaches for precise components are vat photo-polymerisation (VPP) based methods, such as stereolithography (SLA) and digital light processing (DLP). These methods provide unique geometric precision, thin walls (<150 µm), fine features, and high density of resulting ceramics [5-8]. However, mechanical reliability remains critically affected by defect populations influenced by the printing process, the type of suspensions used, the part's design, and thermal post-processing. The critical factors in the manufacturing process are printing orientation, layer thickness, cure depth, and surface topography[9-13]. Therefore, several new potential flaw sources are present compared with classical ceramic manufacturing processes. Recent interlaboratory studies,

* Corresponding author: chlup@ipm.cz (Z. Chlup)

fractographic investigations, and other specific targeted works, such as high-throughput strength methods (e.g., CharAM), show that printing orientation is one of the strongest predictors of failure mode, Weibull modulus, and characteristic strength [10, 11, 14, 15].

The results reported by Maier et al. [10] for alumina revealed differences in print orientation and variations among the 6 labs, despite using the same suspension and flexural strength evaluation procedures. The microstructure of ceramic specimens varied with the location of the printing job, both in grain size and porosity, which can be attributed to deviations in the lab's furnaces. The comparison of all data revealed scatter in the Weibull characteristic strength, ranging from 225 MPa to 378 MPa, corresponding to approximately a 60% difference and mostly below the characteristic strength of conventionally prepared materials, which is 375 MPa. Although observation did not confirm the presence of a layered structure in the printed specimens, horizontally printed specimens exhibited higher strength than vertically printed specimens. The results are similar to those reported in other works [10, 11, 16, 17]. New types of defects have been identified through detailed fractographical analysis, such as wormholes and flat, round pores. These defects originate from bubbles present in the suspension, which either extend across multiple layers or become entrapped within a single layer. At present, they pose a challenge for fracture-mechanical descriptions based on idealised round pores [18-20]. Even though some studies are trying to describe irregular shapes [21, 22].

Although the interface in 3D-printed bodies is not visible, it can still influence mechanical properties and fracture behaviour. Oxygen inhibition during the curing process is well documented [23-25] and depends on factors such as the surrounding atmosphere, the vat surface, and the suspension composition, powder chemistry, and size distribution.

In the case of a multimaterial ceramic VPP-DLP, additional factors come into play, primarily the coefficient of thermal expansion mismatch between the materials, which leads to internal stresses. It can be both an advantage and a disadvantage, as demonstrated in some other works [26, 27].

The investigation in this paper focuses on the description of selected printing parameters (energy and orientation) and their impact on the flexural strength and fracture toughness of single materials. Also, it raises additional issues when Al_2O_3 and ZrO_2 are co-printed as multimaterials.

Experimental

Several experiments were conducted in this study, schematically shown in **Fig. 1a**, to demonstrate the effectiveness of fractographic analysis. Initially, the effect of curing intensity on the strength of green bodies (GB) was analysed for a single layer in the loading orientation. Later, with optimised printing parameters, two printing strategies (horizontally - H and vertically - V) were tested as shown in **Fig. 1b**. Finally, multimaterial experiments in the form of laminated structures were conducted to determine issues such as shrinkage mismatch, defect formation, and cross-contamination.

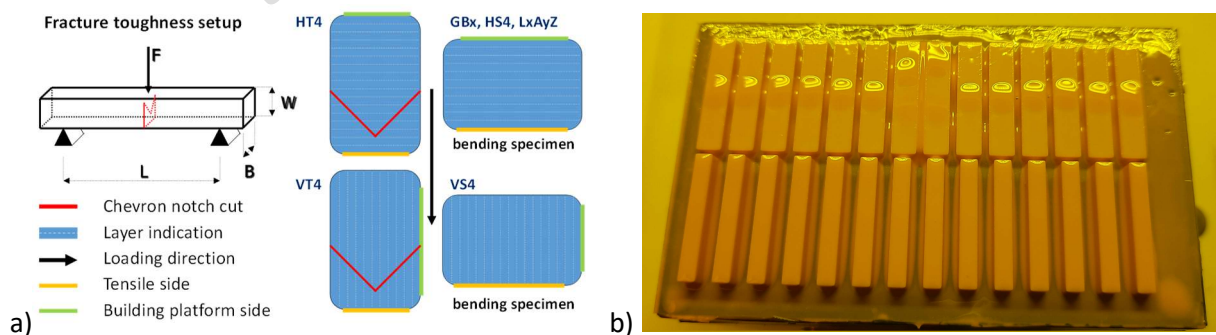


Fig. 1 Schematic of loading setup for fracture toughness, printed specimen geometries and printing orientation to the loading axis for both the fracture toughness (HT4, VT4) and flexural strength specimens, i.e., GBx, HS4, VS4, and LxA:zY (a), and picture of just printed specimens on the building platform showing first row HS4 specimens and last row VS4 specimens (b).

Commercially available suspension LithaLox 350 Alumina (Lithoz, Austria), a representative of widely used Al_2O_3 material, was used for all single-material printing experiments in this study. Multimaterial laminates were produced using a combination of LithaLox 350 Alumina and LithaCon 3Y 210 Zirconia (Lithoz, Austria) with similar solid loading, 49 and 48 vol. %, respectively. All printing experiments were conducted using a multimaterial DLP printer, CeraFab Multi 2M30 (Lithoz, Austria). The energy effect on printed green bodies was investigated over the recommended range 100-400 mJ/cm^2 , with other printing parameters held constant. However, the energy of 100 mJ/cm^2 was found insufficient due to poor adhesion to the building platform when printed without an adhesive layer. The bars were printed with a round chamfer as shown in **Fig. 1a** to eliminate edge stress concentration. The laminates were printed with three material layer thickness ratios, 1:2, 1:1, and 2:1 (see **Table 1**). The printed bodies, with nominal dimensions of 3 mm \times 4 mm \times 20 mm, were removed from the building platform and carefully cleaned with compressed air and cleaning agent LithaSol 20 (Lithoz, Austria).

Table 1: Summarisation table of printing and testing parameters

Serie	Test	LithaLox	LithaCon	Layer	Energy	Intensity	Cross-head	N
		350	3Y 210	thickness			speed	
		[Vol. %]	[Vol. %]	[μm]	[mJ/cm²]	[mW/cm²]	[mm/min]	[-]
Green bodies – Alumina								
GB1	FS-3pb	100	0	25	200	80	0.5	12
GB2	FS-3pb	100	0	25	300	80	0.5	12
GB3	FS-3pb	100	0	25	400	80	0.5	12
Single-materials - Alumina								
HS4	FS-3pb	100	0	25	200	80	0.5	24
VS4	FS-3pb	100	0	25	200	80	0.5	22
HT4	FT-CNB	100	0	25	200	80	0.005	11
VT4	FT-CNB	100	0	25	200	80	0.005	11
Multi-materials - Alumina / Zirconia								
L1A:2Z	FS-3pb	33	66	25	200	80	0.5	4
L1A:1Z	FS-3pb	50	50	25	200	80	0.5	4
L2A:1Z	FS-3pb	66	33	25	200	80	0.5	4

N – number of valid tests, **FS-3pb** – Flexural strength three-point bending test, **FT-CNB** – Fracture toughness Chevron notch beam test.

Binder removal was carried out under N_2 atmosphere, as described by Stastny et al. [12]. During N_2 debinding, the bodies were embedded in granular activated carbon AY-5 12 \times 30 (Carbon Link, UK). A nitrogen flow rate of 20 L/h was maintained during binder removal in the muffle furnace. A heating rate of 0.5 $^\circ\text{C}/\text{min}$ to 500 $^\circ\text{C}$, followed by 1 $^\circ\text{C}/\text{min}$ to 800 $^\circ\text{C}$, was used, followed by controlled cooling (5 $^\circ\text{C}/\text{min}$) to room temperature. Brown bodies were sintered in air. The heating rate was 1 $^\circ\text{C}/\text{min}$ to 780 $^\circ\text{C}$, then 2 $^\circ\text{C}/\text{min}$ to a sintering temperature of 1550 $^\circ\text{C}$, with a 2-hour dwell at this temperature. Controlled cooling at 5 $^\circ\text{C}/\text{min}$ to room temperature was applied. Specimens' geometry was measured using a micrometre (Mitutoyo, Japan) at least three times.

The flexural strength was determined using a three-point bending setup with a span of 16 mm and a roller diameter of 5 mm. For loading, a universal electromechanical testing machine, Instron 8862 (Instron, USA), was employed, with a cross-head speed of 0.5 mm/min for flexural strength and 0.005

mm/min for fracture toughness. A load cell with a maximum capacity of 500 N and an LVDT extensometer with a gauge length of 1mm (both HBM, Germany) were used to record data and construct loading diagrams for further evaluation. The determined flexural strength was evaluated using both the Gaussian and Weibull statistical approaches to determine characteristics, including mean strength, characteristic strength, standard deviation, and Weibull modulus. The validity of this approach for 3D printed materials is discussed [28]. The fracture toughness was determined using the Chevron notch beam technique, employing a Blums slice method to assess the compliance function, as described elsewhere [29, 30]. The obtained data were also statistically treated using Gaussian statistics.

Fracture surfaces of all specimens were documented using optical microscopy, and selected specimens were carbon-coated to be further observed in the scanning electron microscope. The fractographic analysis was conducted using an SEM Lyra3 (Tescan, Czech Republic), employing both secondary and backscattered electron modes.

Results and discussion

Initially, the green bodies obtained by printing under various conditions were characterised using a flexural strength test. The dependence shown in **Fig. 2a** represents the flexural strength as a function of the energy used for curing of the one-material-layer system. The maximum average strength corresponds to an energy of 200 mJ/cm², which was used for all subsequent prints. Also, the flexibility of the specimens decreased by 15%, together with a decrease in the strength at an energy of 400 mJ/cm². Interestingly, higher strength also corresponded to higher specimen precision, as indicated by the dependence of dimensions in **Fig. 2b**. The increasing applied energy led to lateral bleeding, a consequence of light scatter and overcuring in that direction. This phenomenon has been well studied in DLP printing of polymers [31, 32]. The lateral dimension increased by up to 4.5% with increasing energy from 200 to 400 mJ/cm², which can be considered a significant change in dimension because it corresponds to more than 6 printing pixels and influences overall precision. The dimension in the printing direction, i.e., specimen thickness, controlled by the printing layer thickness, was kept constant, as shown in **Fig. 2b**, even though scattering within a few micrometres was observed due to levelling of the building platform. This finding is in good agreement with the literature, where the effects of increasing curing energy on curing depth and dimensional precision show the same trend, but the direct applicability of the literature data is limited by the variation in suspensions used [7, 8].

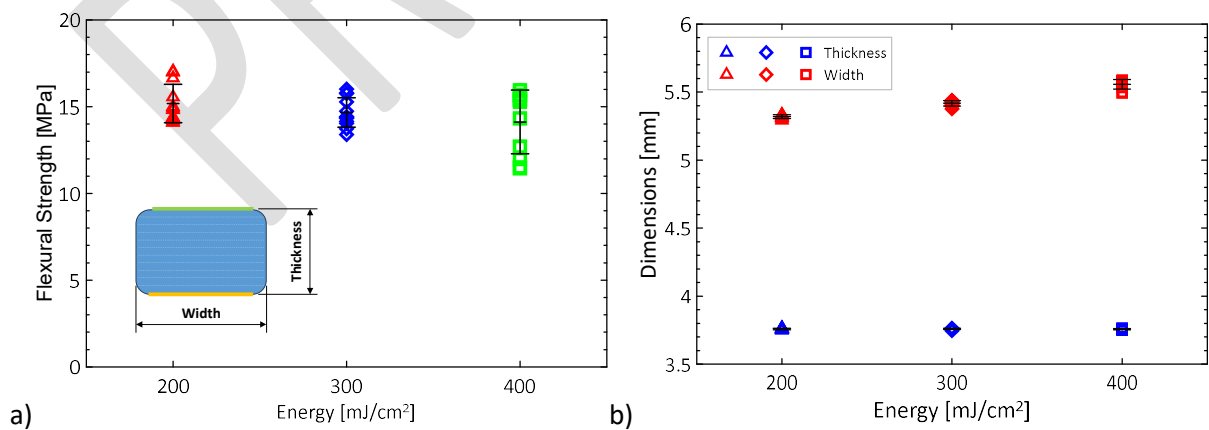


Fig. 2 Dependence of flexural strength (a) and specimen thickness and width (b) on applied energy during printing of green bodies with marked average and standard deviation.

Sintered bodies for flexural strength and fracture toughness tests were prepared under optimal printing conditions with different layer orientations. The relationship between print orientation and loading direction, as shown in **Fig. 3a** and the corresponding Weibull plots in **Fig. 3b**, describes the fracture behaviour of 3D-printed single-materials. The vertically oriented layers exhibit slightly higher average flexural strength (in contrast to slightly lower Weibull strength) and lower scatter. The directional dependence was also described by other authors, as mentioned previously; however, Borlaf et al. reported an effect of printed material, in which ATZ and ZrO₂ exhibited opposite behaviour, which they attributed to the suspension used [17]. Both data sets exhibit deviations from Weibull behaviour, consistent with the hypothesis of bimodal distributions of flaw types, as described by Danzer [28, 33]. A stronger bimodal distribution of flaws is observed in the horizontal orientation. All obtained strength data are consistent with similar experiments reported in the literature [10, 16], i.e., reasonably lower than the strength values obtained on specimens prepared by a conventional manufacturing approach, i.e. cold isostatic pressing followed by free sintering. Note that in DLP printing, the tensile surface of the specimens is in the as-printed state, without any machining. The lower values obtained for as-printed specimens are in line with findings by Bergler et al., who reported higher strength for conventional processing [13].

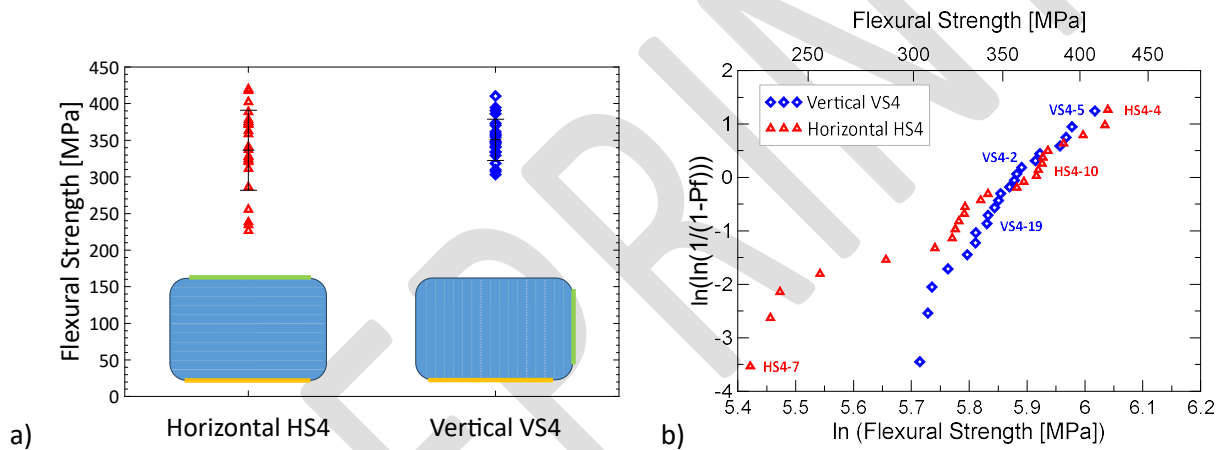


Fig. 3 Dependence of flexural strength on printing to loading orientation (a) and corresponding Weibull plots (b) with marked specimens shown further in fractographic analysis.

Fractographic analysis was conducted to describe the fracture behaviour of DLP-printed material and to reveal typical fracture origins. In the Weibull plots (**Fig. 3b**), selected specimens are marked according to their strength, and the corresponding fracture surfaces with identified fracture origins are shown in **Fig. 4**. In all selected cases, surface defects were identified as fracture origins, differing in size and shape. The fracture of horizontally oriented specimens usually initiates from surface pores. The fracture origin for high-strength specimens (e.g., HS4-4), was a small, round surface pore of size similar to the printing layer thickness. The specimen corresponding to the Weibull strength (e.g., HS4-10) exhibits disk-shaped pore fracture origins with a depth of one printing layer but a much larger lateral size. The weakest specimens (e.g., HS4-7) initiated from large pores that cross several printing layers, known as „wormholes“ [18]. The bimodal flaw size effect visible in the Weibull distribution is due to the limitation of most defects by the printing layer thickness and the presence of several large defects of size defined as the multiplication of the printing layer's thickness, as shown also by Maier [10]. A different situation occurs when the loading-to-printing direction is described as vertical. Fracture origins for high strengths (e.g., VS4-5) were surface defects due to polymerisation processes at edges, creating „waviness“; other crack initiation sites can be in the vicinity of relatively large interlayer cracks formed during debinding or sintering (e.g., VS4-2). Multiple crack initiations from surface and internal initiation sites led to reduced strength values, as shown for specimen VS4-19. The fact that chamfers,

i.e. round edges, were printed, no initiation of fracture occurred from the edge of the bars themselves, which is, on the other hand, typical for sharp or machined chamfers [17, 20].

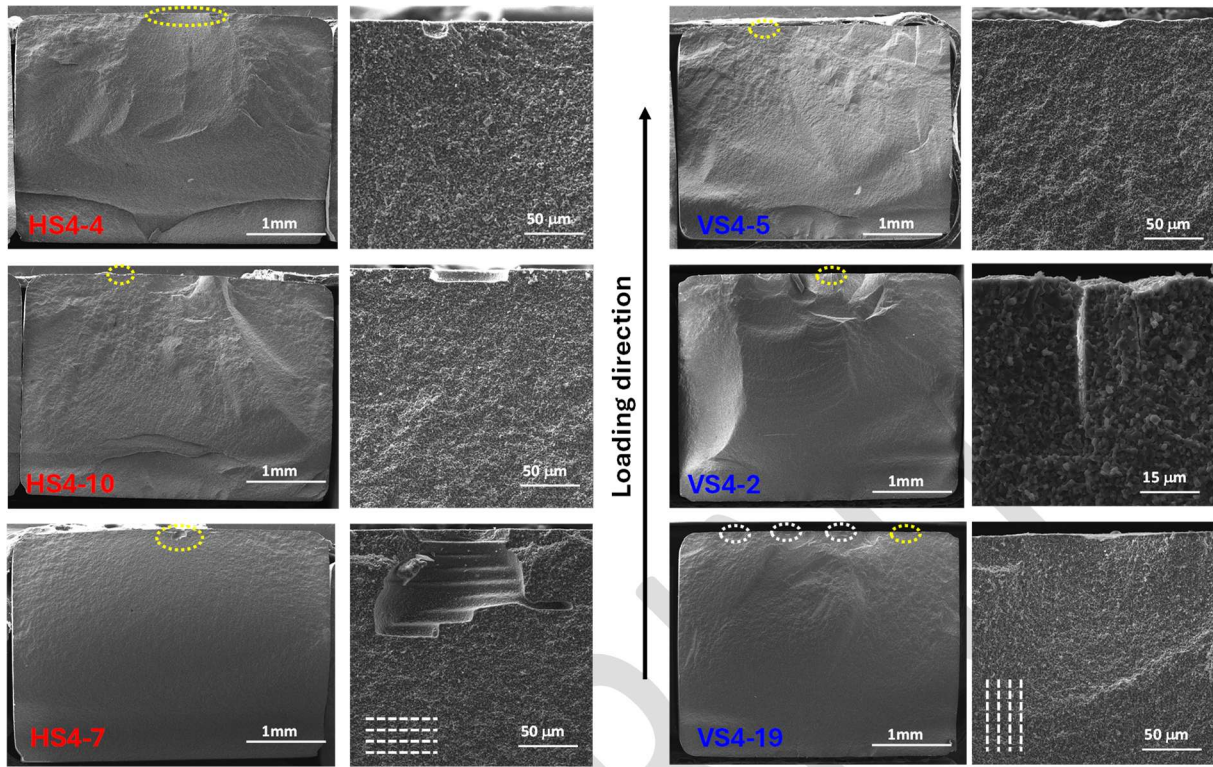


Fig. 4 Examples of fracture surfaces of selected horizontally (left) and vertically (right) printed specimens. Fracture origins: HS4-4 – surface round pore, HS4-10 – large “disc-shaped” pore with thickness of one layer, HS4-7 – large pore „wormhole” through several layers, VS4-5 – surface valley, VS4-2 – surface interlayer crack, and VS4-19 – multiple surface flows. The yellow ellipse indicates the initiation site, which is shown in detail.

The fracture toughness determined using the Chevron notch technique revealed an opposite trend to that of flexural strength. The datasets for each orientation are shown in **Fig. 5a**, where the highest fracture toughness was observed for a crack propagating perpendicular to the plane of the printing layer. Additionally, the scatter in this case was smaller than in the vertical arrangement. The main results of the fractographical analysis are presented in **Fig. 5b**, where examples of fracture surfaces from invalid tests (showing incorrect loading curves, VT4-3 and HT4-2) exhibit interlaminar cracks that significantly affect crack initiation and propagation from the Chevron notch. The fracture surfaces of valid experiments are shown for specimens VT4-10 and HT4-6 for comparison.

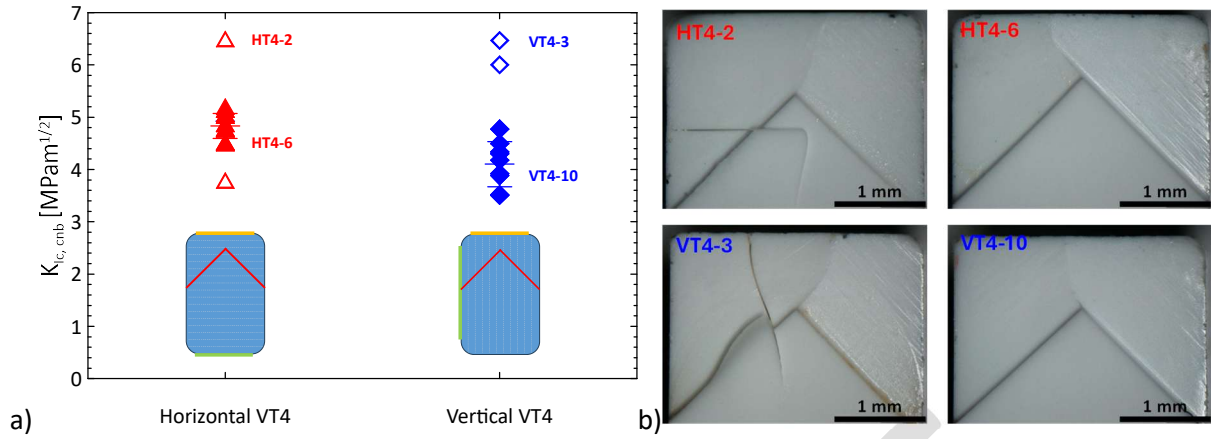


Fig. 5 Dependence of fracture toughness on printing to loading orientation (a) and optical images of fracture surfaces of selected specimens (b) of sintered Al_2O_3 bodies. Invalid fracture toughness data are in the graph shown by empty symbols.

The dependence of the flexural strength data of all tested laminated specimens is plotted in **Fig. 6a**. The multimaterial $\text{Al}_2\text{O}_3/\text{ZrO}_2$ specimens exhibited higher flexural strength than the single-material Al_2O_3 specimens in all cases, compared with **Fig. 3**. There are two reasons for this behaviour. One is the higher strength of zirconia itself, and the second is the presence of internal stresses developed during sintering, as described here [34, 35]. For the observation of fracture surfaces of laminates, both secondary (SE) and backscattered (BSE) electrons, the second were used to distinguish between the two materials, as shown in **Fig. 6b**. Presented images of Al_2O_3 layer at various stages of multimaterial printing demonstrate a significant problem in multimaterial DLP printing: cross-contamination closely linked to the cleaning process during vat switching [36, 37]. The situation in the one of the first deposited multimaterial layers is shown in the top part of **Fig. 6b**, and the analogous image after several layers is shown in the bottom part. The visible zirconia particles in the alumina layer are a sign of the cross-contamination event, although zirconia particles are not entirely spread in the alumina layer thickness. They are concentrated in the first half, indicating improper cleaning and some remaining uncured suspension from the previously deposited layer.

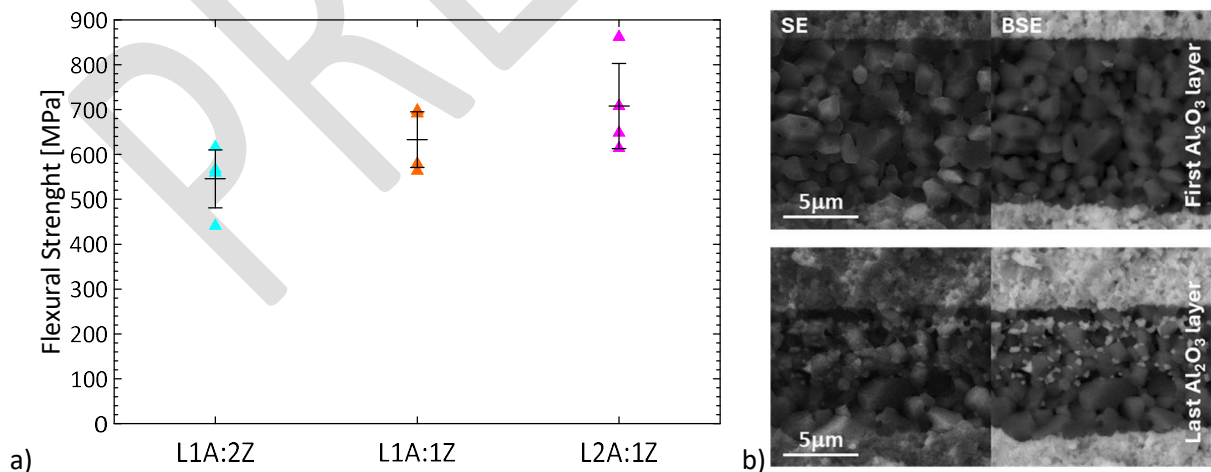


Fig. 6 Comparison of flexural strength data obtained for the multi-material laminates (a) and a detailed view of fracture surfaces of selected laminates with focus on alumina layer (dark phase) at the beginning (up) and at the end (down) of printing, showing significant cross-contamination by zirconia particles (white phase) for later stages of printing (b).

An overall summary of flexural strength values determined using the Gaussian and Weibull statistics for both green bodies, single-material ceramics, and laminates is presented in **Table 2**. For laminates, because of the small number of values, only Gaussian statistics are used. The average fracture toughness with its standard deviation (SD), calculated only from valid values, is also included.

Table 2: Summary table of flexural strength and fracture toughness

Serie	Gaussian		Weibull		Fracture toughness	
	σ_{avg}	SD	σ_w	m	$K_{Ic, cnb}$	SD
	[MPa]	[MPa]	[MPa]	[MPa]	[MPa·m ^{1/2}]	[MPa·m ^{1/2}]
Green bodies – Alumina						
GB1	15.2	1.1	15.7	14.1	-	-
GB2	14.7	0.9	15.1	19.0	-	-
GB3	14.4	2.0	15.2	9.3	-	-
Single-materials - Alumina						
HS4/HT4	336	55.8	359	7.6	4.1	0.4
VS4/VT4	351	28.9	345	23.3	4.9	0.3
Multi-materials - Alumina / Zirconia						
L1A:2Z	546	74.4	-	-	-	-
L1A:1Z	633	71.5	-	-	-	-
L2A:1Z	708	109.7	-	-	-	-

Fractographic analysis of 3D printed multimaterial ceramics reveals several defect types that differ from those described for single-material specimens; however, some of them have a similar origin, as shown in **Fig. 7a**. A disk-shaped surface pore formed due to the presence of a bubble in the suspension that was entrapped in the layer. Uneven layer thicknesses and differences in the cross-contamination depending on the material used, shown in **Fig. 7b**, are another feature identified when multimaterial printing is applied. It is most likely caused by improper cleaning of the surface of the already-printed layer, resulting in some waviness. The different curing appears visible at the edges, creating artificial stress concentrators, as well as layer deformation during cleaning of the multilayer specimen, depending on the local cleaning forces applied (**Fig. 7c**). Another artefact created during the cleaning and its effect on the fracture process is shown in **Fig. 7d**, where a fibre from the cleaning tissue was integrated into the printed body. During the debinding and sintering steps, the organic fibre decomposed and evaporated, forming an elongated pore that probably traversed several layers. A detailed image of the pore with visible imprinted fibre structure is shown in **Fig. 7e**. Another defect type was the mixing of places where individual materials were combined. This can likely be explained by the non-ideal adhesion of the previous layer of material A, the removal of a small fragment of material A, or the formation of a pore formed by a bubble in the suspension. The resulting gap is subsequently filled with material B, creating a recess in the underlying layer of material A (see **Fig. 7f**). Similar defects, as shown for multi-material systems, can occur in single materials, but they are difficult or impossible to detect. The reason for insufficient attachment of the layer can be in the presence of bubbles or oxygen inhibition of the previous layer surface, which prohibits sufficient adhesion of layers from dissimilar materials.

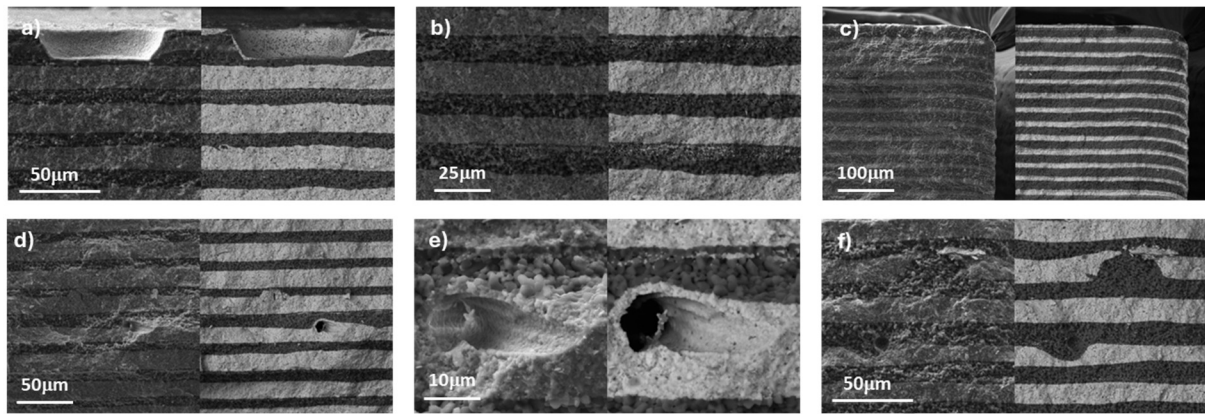


Fig. 7 Examples of defects found at the fracture surfaces of selected laminates, the large “disc-shaped” pore (a), significant unevenness of layer thickness and cross-contamination (b), “bending” of layers at edges (c), damage around a large pore crossing layers (d), detail of the pore (e), and effect of refilling gaps or pores by other material (f).

Successful multimaterial printing requires modifying the suspension's rheology, solid loading, and curing properties to mitigate most of the described issues as shown for zirconia with various amounts of yttria [13]. Bergler's use of similar materials simplifies the situation, unlike the one investigated here. The comparable rheological properties of the suspensions ensure an effective cleaning process and eliminate mixing of uncured suspensions. The solid loading being at the same level (49 vs 48 vol.%) ensured comparable shrinkage during debinding and, subsequently, positively influenced the co-sintering of dissimilar materials. The similar curing properties eliminate surface waviness caused by overcuring of one material and potentially insufficient curing of the other. This issue will depend heavily on the selected materials, the powder particle size, the curing agent, the absorber content in the suspension, and the resulting individual curing depths, which were not available for the commercial suspensions used.

Conclusions

Processing parameters, particularly the curing energy/intensity, critically influence the 3D printed green body's mechanical properties, dimensional accuracy, and consequently debinding/sintering behaviour. An optimal exposure level of 200 mJ/cm² was identified for a used alumina suspension within the analysed range, whereas higher energies promote lateral overcuring and geometric distortion without improving manipulation strength or flexibility.

The mechanical behaviour of sintered DLP-printed ceramics is governed by the interplay among process parameters, defect size distribution, and the quality of printed layer interfaces. Loading-to-printing direction significantly affects performance, as evidenced by printing defects, confirming the intrinsic anisotropy of the printed microstructure. The strength of ≈ 350 MPa was similar to that reported in other 3D-printing studies but was just below that of conventionally prepared alumina materials. Fractographic analysis revealed that the fracture is controlled predominantly by surface and/or printing interlayer defects, including pores of varying morphologies, such as round, disk-shaped, and wormhole shapes. The edge stress concentration and, therefore, edge-fracture initiation were successfully eliminated by printed rounded edges. The observed deviations from the ideal Weibull behaviour in the flexural strength are consistent with bimodal flaw populations, reflecting the coexistence of process-induced defect types of strictly defined/limited sizes within a single layer.

3D printed multimaterial Al₂O₃/ZrO₂ laminates exhibit improved flexural strength up to 700 MPa relative to alumina due to phase combination and residual stress development during densification.

However, their reliability is limited by cross-contamination, non-uniform layer formation, and defects associated with the cleaning process required between material alternation. Some of the described defects can also be present in single-material prints. For reliable multimaterial DLP processing, matching suspension rheology, solid loading, and curing behaviour, along with an enhanced cleaning process that eliminates cross-contamination, is essential to minimise interfacial defects and ensure consistent co-sintering. These findings provide a framework for optimising the AM of ceramics to improve mechanical reliability.

Acknowledgement

The research was supported by the project “Mechanical Engineering of Biological and Bio-inspired Systems”, project No. CZ.02.01.01/00/22_008/0004634, Programme Johannes Amos Comenius, call Excellent Research. We acknowledge CzechNanoLab Research Infrastructure (ID 90251), supported by MEYS CR.

CRedit authorship contribution statement:

Conceptualisation: ZC; PS; data curation: ZC; PS; formal analysis: ZC; PS; FS; LB; VM; DD; funding acquisition: ZC; investigation: ZC; PS; HH; FS; LB; OS; VM; DD; methodology: ZC; PS; HH; DD; validation: ZC; HH; DD; writing – original draft: ZC; PS; HH; FS; VM; DD; writing – review & editing: ZC; PS; HH; FS; LB; OS; VM; DD.

Data Availability

Data related to the paper are available in the Zenodo repository with <https://doi.org/10.5281/zenodo.19604273>

References

- [1] Z. Chen, Z. Li, J. Li, C. Liu, C. Lao, Y. Fu, C. Liu, Y. Li, P. Wang, Y. He, 3D printing of ceramics: A review, *Journal of the European Ceramic Society* 39(4) (2019) 661-687.
- [2] R.B. Osman, A.J. van der Veen, D. Huiberts, D. Wismeijer, N. Alharbi, 3D-printing zirconia implants; a dream or a reality? An in-vitro study evaluating the dimensional accuracy, surface topography and mechanical properties of printed zirconia implant and discs, *Journal of the Mechanical Behavior of Biomedical Materials* 75 (2017) 521-528.
- [3] M.H. Razzaq, M.U. Zaheer, H. Asghar, O.C. Aktas, M.F. Aycan, Y.K. Mishra, Additive manufacturing for biomedical bone implants: Shaping the future of bones, *Materials Science and Engineering: R: Reports* 163 (2025) 100931.
- [4] G. Zhang, B. Zou, X. Wang, Y. Yu, C. Huang, H. Zhu, P. Yao, H. Liu, The 3D-Printed building and performance of Al₂O₃ ceramic filters with gradient hole density structures, *Ceramics International* 49(19) (2023) 31496-31508.
- [5] S. Wu, R. Wang, L. Jin, X. Huang, W. Li, K. Zhou, Q. Ge, Digital light processing 3D printing of large-scale and crack-free ceramics with perforated internal honeycomb structures, *Virtual and Physical Prototyping* 20(1) (2025) e2589472.
- [6] X. Yu, Z. Wang, Q. Li, Y. Zhao, J. Zhao, Spatial curing growth mechanism and defect control of alumina green bodies manufactured by stereo-lithography, *Journal of the European Ceramic Society* 42(6) (2022) 2931-2945.
- [7] N. Butler, Y. Zhao, S. Lu, S. Yin, Effects of light exposure intensity and time on printing quality and compressive strength of β -TCP scaffolds fabricated with digital light processing, *Journal of the European Ceramic Society* 44(4) (2024) 2581-2589.

- [8] C.L. Cramer, J.K. Wilt, Q.A. Campbell, L. Han, T. Saito, A.T. Nelson, Accuracy of stereolithography printed alumina with digital light processing, *Open Ceramics* 8 (2021) 100194.
- [9] S. Zhou, F. Zhang, J. Wu, J. Su, K. Liu, Y. Zhang, C. Wang, C. Yan, Y. Shi, Anisotropy in ceramic vat photopolymerization: Formation mechanisms, influence on properties, and manipulating strategies, *Journal of the European Ceramic Society* 45(7) (2025) 117249.
- [10] R.A. Maier, A.J. Allen, B. Cox, I. Levin, Interlaboratory study of flexural strength in additively manufactured alumina, *Journal of the American Ceramic Society* 108(2) (2025) e20133.
- [11] T. Lube, M. Staudacher, A.-K. Hofer, J. Schlacher, R. Bermejo, Stereolithographic 3D Printing of Ceramics: Challenges and Opportunities for Structural Integrity, *Advanced Engineering Materials* 25(7) (2023) 2200520.
- [12] P. Stastny, O. Man, D. Brouczek, M. Schwentenwein, M. Trunec, Effect of atmosphere on thermal debinding of DLP-printed ceramics, *Journal of the European Ceramic Society* 46(3) (2026) 117891.
- [13] M. Bergler, A. König, J. Korostoff, F.K. Mante, S. Hahnel, M. Rosentritt, Comparison of the flexural strength and microstructure of 3D printed and milled mono- and multilayer zirconia, *Journal of the Mechanical Behavior of Biomedical Materials* 177 (2026) 107370.
- [14] M. Staudacher, U. Scheithauer, M. Reichel, N. Lorenz, M. Schwentenwein, T. Lube, Strength testing of additive manufactured ceramics – A round robin using the CharAM-methodology, *Open Ceramics* 17 (2024) 100557.
- [15] M. Staudacher, T. Lube, J. Glettler, U. Scheithauer, M. Schwentenwein, A novel test specimen for strength testing of ceramics for additive manufacturing, *Open Ceramics* 15 (2023) 100410.
- [16] J. Schlacher, T. Lube, W. Harrer, G. Mitteramskogler, M. Schwentenwein, R. Danzer, R. Bermejo, Strength of additive manufactured alumina, *Journal of the European Ceramic Society* 40(14) (2020) 4737-4745.
- [17] M. Borlaf, L. Conti, T. Graule, Influence of tensile edge design and printing parameters on the flexural strength of ZrO₂ and ATZ bars prepared by UV-LCM-DLP, *Open Ceramics* 5 (2021) 100066.
- [18] W. Harrer, M. Schwentenwein, T. Lube, R. Danzer, Fractography of zirconia-specimens made using additive manufacturing (LCM) technology, *Journal of the European Ceramic Society* 37(14) (2017) 4331-4338.
- [19] J.J. Mecholsky, S.W. Freiman, R.W. Rice, Fracture surface analysis of ceramics, *Journal of Materials Science* 11(7) (1976) 1310-1319.
- [20] G. Quinn, NIST Recommended Practice Guide: Fractography of Ceramics and Glasses, 3rd edition, Special Publication (NIST SP), National Institute of Standards and Technology, Gaithersburg, MD, 2020.
- [21] X. Zhao, A. Wang, Y. Chen, Q. Zheng, S. Wang, Quantitative strength prediction of advanced ceramics with regular/irregular flaws in I-mode failure condition, *Ceramics International* 47(22) (2021) 31527-31535.
- [22] A. Wang, X. Zhao, M. Huang, Z. Zhang, L. Xie, A quantitative study of flaw/strength response in ultra-high temperature ceramics based on femtosecond laser method, *Theoretical and Applied Fracture Mechanics* 110 (2020) 102775.
- [23] Y. Zhang, H. de Haan, K. Houlahan, K.L. Sampson, D. Webber, A. Orth, T. Lacelle, L. Gaburici, R. Lam, B. Deore, C. Paquet, Impact of oxygen inhibition on (meth)acrylate photopolymerization in tomographic volumetric printing, *Additive Manufacturing* 109 (2025) 104844.
- [24] J.R. Tumbleston, D. Shrivanyants, N. Ermoshkin, R. Januszewicz, A.R. Johnson, D. Kelly, K. Chen, R. Pinschmidt, J.P. Rolland, A. Ermoshkin, E.T. Samulski, J.M. DeSimone, Continuous liquid interface production of 3D objects, *Science* 347(6228) (2015) 1349-1352.
- [25] Q. Cao, Y. Liu, S. Yong, L. Su, J. Liao, X. Li, X. Zhu, A novel oxygen inhibition strategy for improving the printability of small-size features in DLP-printed CaP ceramic scaffolds, *Materials & Design* (2026) 115999.
- [26] R. Bermejo, P. Supancic, I. Kraveva, R. Morrell, R. Danzer, Strength reliability of 3D low temperature co-fired multilayer ceramics under biaxial loading, *Journal of the European Ceramic Society* 31(5) (2011) 745-753.

- [27] J. Schlacher, S. Geier, M. Schwentenwein, R. Bermejo, Towards 3D-printed alumina-based multi-material components with enhanced thermal shock resistance, *Journal of the European Ceramic Society* 44(4) (2024) 2294-2303.
- [28] R. Danzer, P. Supancic, J. Pascual, T. Lube, Fracture statistics of ceramics – Weibull statistics and deviations from Weibull statistics, *Engineering Fracture Mechanics* 74(18) (2007) 2919-2932.
- [29] J.I. Bluhm, Slice synthesis of a three dimensional “work of fracture” specimen, *Engineering Fracture Mechanics* 7(3) (1975) 593-604.
- [30] Z. Chlup, D.N. Boccaccini, C. Leonelli, M. Romagnoli, A.R. Boccaccini, Fracture behaviour of refractory ceramics after cyclic thermal shock, *Ceramics-Silikaty* 50(4) (2006) 245-250.
- [31] J. Bonada, A. Muguruza, X. Fernández-Francos, X. Ramis, Influence of exposure time on mechanical properties and photocuring conversion ratios for photosensitive materials used in Additive Manufacturing, *Procedia Manufacturing* 13 (2017) 762-769.
- [32] T.J. Kolibaba, J.P. Killgore, B.W. Caplins, C.I. Higgins, U. Arp, C.C. Miller, D.L. Poster, Y. Zong, S. Broce, T. Wang, V. Talačka, J. Andersson, A. Davenport, M.A. Panzer, J.R. Tumbleston, J.M. Gonzalez, J. Huffstetler, B.R. Lund, K. Billerbeck, ..., X. Zhao, Results of an interlaboratory study on the working curve in vat photopolymerization, *Additive Manufacturing* 84 (2024) 104082.
- [33] R. Danzer, On the relationship between ceramic strength and the requirements for mechanical design, *Journal of the European Ceramic Society* 34(15) (2014) 3435-3460.
- [34] Z. Chlup, H. Hadraba, D. Drdlik, K. Maca, I. Dlouhy, R. Bermejo, On the determination of the stress-free temperature for alumina-zirconia multilayer structures, *Ceramics International* 40(4) (2014) 5787-5793.
- [35] Z. Chlup, H. Hadraba, L. Slabakova, D. Drdlik, I. Dlouhy, Fracture behaviour of alumina and zirconia thin layered laminate, *Journal of the European Ceramic Society* 32(9) (2012) 2057-2061.
- [36] I.A. Sutejo, S. Zhang, C.W. Gal, Y.-J. Choi, H. Park, H.-S. Yun, Stamping cleaning conception on cross-contamination free multi-ceramic bioglass-tricalcium phosphate core-shell structure fabrication, *Materials & Design* 246 (2024) 113304.
- [37] J. Cheng, S. Yu, R. Wang, Q. Ge, Digital light processing based multimaterial 3D printing: challenges, solutions and perspectives, *International Journal of Extreme Manufacturing* 6(4) (2024) 042006.